

Photometric Behavior of the Cataclysmic Variable SDSS J150240.98+333423.9/NZ Boo in Quiescence

T. S. Khruzina* and I. B. Voloshina

*Sternberg Astronomical Institute, Lomonosov Moscow State University,
Universitetskii pr. 13, Moscow, 119992 Russia*

Received September 23, 2014; in final form, December 19, 2014

Abstract—An analysis of V photometric light curves of the eclipsing cataclysmic variable SDSS J150240.98+333423.9/NZ Boo obtained in April–June, 2012 with a CCD photometer using the 60-cm telescope of the Sternberg Astronomical Institute’s Crimean station is presented (based on more than 750 images). The first observation was made ~ 350 – 370 orbital cycles after the beginning of the outburst of April 2012; all the observations correspond to quiescence of the system. The orbital period, $P = 0.0589106(4)^d$, changed by no more than $\Delta P_{\text{orb}}/P_{\text{orb}} \sim 2 \times 10^{-5}$ during the more than 37 200 orbital cycles since the previous observations of the system. The light curves of SDSS J150240.98+333423.9 folded with the orbital period reveal variations of the eclipse depth by up to $\sim 1^m$, of the system’s out-of-eclipse brightness level by up to $\sim 0.3^m$, and of the flux around the orbital hump by up to $\sim 0.3^m$. Parameters of the system (its accretion disk, hot line, hot spot, and other components) are derived in a combined model for a cataclysmic variable that takes into account radiation from both the hot line and a hot spot on the leeward side of the gas stream. Analysis of variations of the resulting disk parameters (its radius R_d , α_g , temperature T_{in} in the boundary layer) testifies to changes in these parameters between outbursts: just after the end of the outburst (1–140 orbital cycles), the disk’s radius and the temperature in its inner regions decreased and the radial temperature distribution approached that for the stationary case; after another $\sim 600 P_{\text{orb}}$, the opposite situation was observed.

DOI: 10.1134/S1063772915050042

1. INTRODUCTION

SU UMa stars are a subtype of dwarf novae. In addition to frequent ordinary, or normal, outbursts, they also exhibit outbursts with higher amplitudes and longer durations, called “superoutbursts.” During superoutbursts, “superhumps” appear in the light curves—brightenings of the system during a limited part of its orbital curve that are repeated with a period P_{sh} that is several percent longer than the system’s orbital period P_{orb} . The amplitudes of the superhumps are $\sim 0.3^m$. The orbital periods of SU UMa stars are between 80 and 180 min. Further subdivision into groups within the subtype is also possible: WZ Sge stars have short superhump periods, low superhump amplitudes ($\sim 0.07^m$), and very long time intervals between outbursts (~ 10 years), and ER UMa stars have shorter intervals between their superoutbursts, with normal outbursts occurring every 4 days.

The superhump phenomenon is a characteristic property of SU UMa stars, but these systems also demonstrate certain differences: while both kinds of outbursts are observed for some variables of this type,

others exhibit superoutbursts only; the shapes of the superoutbursts vary strongly not only with the outburst phase, but also from system to system. Extensive observations of such systems have revealed the following [1]. First, the superhump period can vary during an outburst. Second, three stages are observed in the evolution of superhump periods: the early evolution stage (stage A) is characterized by a longer superhump period; the superhump period systematically changes during the transition, or intermediate, stage (stage B); and shorter and stable superhump periods are typical of the last stage (stage C). These stages can be traced best for WZ Sge systems.

The aim of this study is to obtain high-quality photometry of the SU UMa system SDSS J150240.98+333423.9, plot detailed light curves for the various stages, study the system’s variability during quiescence, i.e., in the interval between outbursts, in order to determine the nature of this variability, determine the system’s main parameters in a model for a cataclysmic variable in quiescence, and compare theoretical synthetic light curves with observations.

Section 2 presents a brief description of this system and results obtained from earlier observa-

*E-mail: kts@sai.msu.ru

tions. Section 3 describes the observing material we have obtained. Section 4 is devoted to the orbital ephemeris used to calculate the phases for our observations. Section 5 describes the light curves of SDSS J150240.98+333423.9 based on new V -band photometry and the calculated phases. Section 6 gives a detailed description of the close-binary model used to determine the system parameters, and Section 7 contains the results derived from our modeling. The results of our study are discussed in Section 8, and Section 9 summarizes our main conclusions.

2. MAIN PROPERTIES OF THE SYSTEM

The system SDSS J150240.98+333423.9/NZ Boo (called J1502 below) was identified as a new cataclysmic variable in the course of the Sloan Digital Sky Survey (SDSS), during the fifth year of the project [2]. The system's light curve suggested a high orbital inclination: eclipses with depths to 2.5^m that are repeated with a period of 84.24 min. In addition, spectroscopic observations revealed strong variations of the red and blue components of spectral lines during the orbital cycle, typical of high-inclination systems. The light curve has a plateau before the eclipse ingress, suggesting the absence of a strong hot spot at the point where the gas flow intersects the disk.

After the detection of superoutbursts of J1502 with durations of about 16 days and outburst amplitudes of at least 3.9^m in July 2009, as well as superhumps in the light curves with peak-to-peak amplitudes of up to 0.35^m near the outburst maximum, the system was suspected of being a SU UMa dwarf novae [3]. The mean superhump period for the first four days of the outburst was $P_{sh} = 0.06028^d(19)$, increasing at the rate $\dot{P}_{sh} = (2.8 \pm 1.0) \times 10^{-4}$ during the outburst. The superhump period excess is $\epsilon = 0.023(3)$. The eclipse duration at the median intensity decreased from its largest value of 10.5 min at the outburst maximum to 3.5 min towards its end. During the same time interval, the eclipse depth increased from 0.9^m to 2.1^m . The eclipse duration in quiescence did not exceed 2.7 min, while eclipse depth was 2.8^m .

The following magnitudes were obtained for J1502 during the SDSS project [2]: $u = 17.86^m$, $g = 17.57^m$, $r = 17.68^m$ (effective wavelengths $\lambda\lambda$ 3551, 4686, and 6166 Å, respectively). The system's brightness varied between 13.7^m and 19.6^m during these observations.

The following ephemeris was derived from an analysis of eclipse timings for March 1–10, 2006 [4]:

$$\begin{aligned} \text{Min. phot.} = & \text{BHJD } 2453799.140607(3) \quad (1) \\ & + 0.05890961(5)E; \end{aligned}$$

supplementing those data with eclipse timings obtained during the superoutburst of 2009 [3] yields the orbital ephemeris

$$\begin{aligned} \text{Min. phot.} = & \text{HJD } 2453849.94908135(2) \quad (2) \\ & + 0.05890946(5)E. \end{aligned}$$

Time-resolved photometry [4, 5] performed during the system's quiescence made it possible to determine the main parameters of the system using the method described in [6], based on the following considerations. The secondary (donor) completely fills its Roche lobe ($\mu = 1$); the width of the white dwarf's eclipse depends only on the orbital inclination i and mass ratio $q = M_{wd}/M_{red}$; the gas stream follows a ballistic trajectory from the secondary; and the position of the hot spot depends solely on q and the outer disk radius R_d . Knowing the ingress and egress times of the hot-spot eclipse and the width of the white dwarf's eclipse, it is possible to obtain three relations that can be solved simultaneously to determine q , i , and R_d . The mass of the primary is calculated from its radius, assuming the validity of the empirical relation between the mass and radius of a white dwarf and the corresponding effective temperature [6]. The white dwarf's radius is determined from the duration of the eclipse ingress and egress. The fluxes in the u , g , r bands measured during the white dwarf's eclipse ingress (egress) can be used to derive rough estimates of the effective temperature of the star in the applied model. However, the resulting temperature of the star is higher than expected based on data for its age, possibly due to longitudinal heating of matter as it is transferred to the white dwarf. Table 1 presents the parameters of J1502 derived in [4, 5].

3. OBSERVATIONS

We began our observations of the cataclysmic variable J150240.98+333423.9 when we received information that an outburst of the system had begun on April 1, 2012 from the Japanese site VSNET [7, 8]. We also began photometric monitoring, but our first observations were obtained only on April 23, 2012, due to poor weather conditions.

Our observations were obtained using a CCD photometer on the 60-cm telescope of Moscow State University's Crimean station. The Apogee-47 CCD camera used has a field of view of 528×512 pixels, with a pixel size of $12 \mu\text{m}$. The duration of each series of observations was weather dependent, and varied between 3.5 and 7 hours. The exposure time was 120 s. Our observations cover six nights in April–June 2012; in total, we obtained more than 750 images in the V filter. The uncertainty of our V observations is about 4–5%. The time resolution was 133–135 s.

Table 1. Parameters of J1502 according to [4, 5]

Parameter	Value	Parameter	Value
P_{orb} , min	84.82984 ± 0.00007	a_0 , R_{\odot}	0.5844 ± 0.0013
i , deg	88.35 ± 0.17	K_{wd} , km/s	50.4 ± 0.4
$q = M_{wd}/M_{\text{red}}$	9.078 ± 0.145	K_{red} , km/s	456.5 ± 0.8
M_{wd} , M_{\odot}	0.709 ± 0.004	R_d , a_0	0.280 ± 0.004
M_{red} , M_{\odot}	0.0781 ± 0.0008	T_{wd} , K	11800 ± 1200
R_{wd} , R_{\odot}	0.01145 ± 0.00005	T_{red} , K	2260 ± 300
R_{wd} , a_0	0.0196 ± 0.0002	d , pc	175 ± 11
R_{red} , R_{\odot}	0.1241 ± 0.0003	\dot{M}_{red} , M_{\odot}/year	10.4 ± 0.2

a_0 is the distance between the centers of mass of the system components; K_{wd} , K_{red} are the amplitudes of the radial-velocity curves for the white dwarf and the secondary; d is the distance to the system.

Table 2. Log of observations of J1502 in 2012

I	$N_{(3)}$	$\varphi_{(2)}$	Date, 2012	T_1, T_2 , JD 2456000+	φ_1/φ_2	T_n , JD 2456000+	N	V_{max}	V_{min}
1	0	37200.933	04.23	41.29059–41.57370	0.52/5.33	41.4359625	180	17.183	20.455
2	86	37287.934	04.28	46.39602–46.57318	0.18/3.19	46.5611288	111	17.256	20.835
3	103	37302.935	04.29	47.44047–47.57221	0.91/3.15	47.4448449	85	17.340	20.076
4	137	37337.941	05.01	49.43847–49.57198	0.82/3.09	49.5070208	78	17.253	20.709
5	662	37862.958	06.01	80.29979–80.54155	0.68/4.78	80.4354891	157	17.204	20.383
6	677	37877.949	06.02	81.30325–81.52340	0.72/4.46	81.3186162	145	16.984	19.717

I is an ordinal number for a given set of observations and nightly-mean light curve; $N_{(3)}$ cycle numbers according to (3); $\varphi_{(2)}$ phases of minima according to (2); T_1, T_2 the times of the beginning and end of the eclipse; φ_1, φ_2 the beginning and end phases of the observations according to (3); T_n the refined time of the observed minimum; N the number of CCD frames taken during the night; and V_{max} and V_{min} the maximum and minimum magnitudes in the corresponding set.

The comparison star used has the coordinate $\alpha = 15^{\text{h}}02^{\text{m}}28.54^{\text{s}}$, $\delta = 33^{\circ}32'43.3''$ and the magnitudes $B = 16.583 \pm 0.023$, $V = 16.066 \pm 0.014$, and lies in the immediate vicinity of J1502 (No. 161 in the AAVSO list of standards for the system). We verified that the brightness of this standard was constant using several check stars.

We reduced the observations using the aperture photometry method and the MAXIM-DL standard software package. Further information about our observations is presented in Table 2.

4. ORBITAL EPHEMERIDES

Using the ephemeris from [5] to determine the orbital phases for our observations of J1502, we detected a systematic shift of the primary minimum times to phases $\varphi \sim 0.933 - 0.949$; i.e., $O - C = -(0.0025^{\text{d}} - 0.0040^{\text{d}})$. This shift could be due to a change in the orbital period (Fig. 1): more than

37 200 orbital cycles elapsed between the time of the minimum in the ephemeris [5] and the epoch of our observations, and the orbital period could have changed with the system's evolutionary development.

To improve the ephemeris, we independently searched for the orbital period of J1502 using the 2012 observations. Power spectra were found using code written by V.P. Goranskii, based on the Lafler–Kinman method and been kindly provided by the author. Our period search was carried out in the range $P_{\text{orb}} \sim 0.055^{\text{d}} - 0.065^{\text{d}}$ (i.e., for frequencies $\nu = P^{-1} \sim 15.4 - 18.2 \text{ d}^{-1}$), in steps of 0.002^{d} . Figure 2 displays the power spectrum derived using all the V observations obtained between JD 2456041 and JD 2456081. The maximum power is at $\nu = 16.974874 \text{ d}^{-1}$, corresponding to the period $P = 0.0589106(4)^{\text{d}}$. We adopted JD 2456041.4359625 for the epoch of minimum, which corresponds to the “improved” middle of the third minimum during

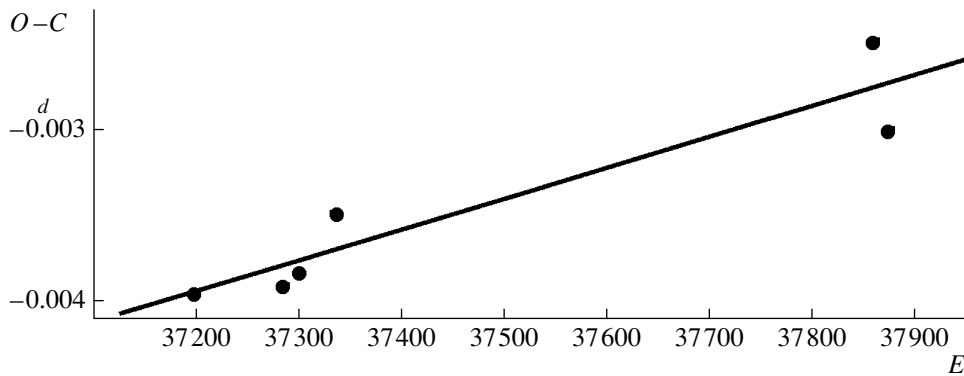


Fig. 1. Dependence of $O-C$ on the orbital cycle number E for the ephemeris (2).

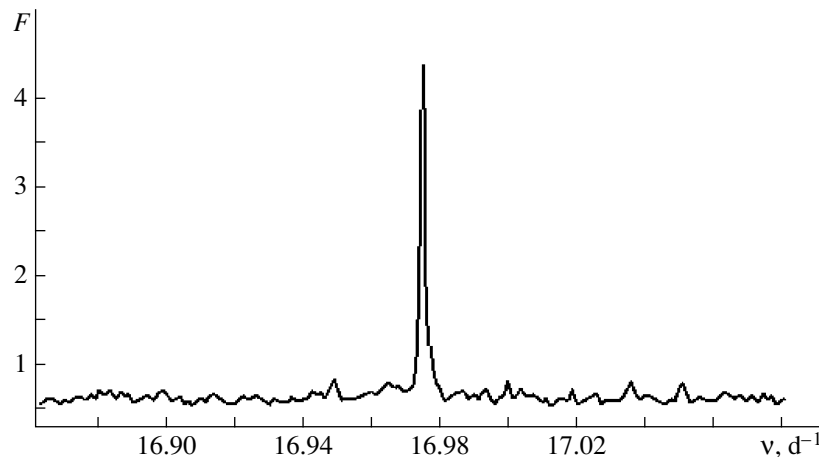


Fig. 2. Power spectrum from observations of J1502 in 2012.

our first observing night (see below concerning the computational technique).

Accurate determination of the time of the minimum corresponding to the middle of the eclipse of the white dwarf by the secondary requires observations with high time resolution. In this case, features in the light curve can be used to reliably determine the epochs of the ingress and egress of the white dwarf's eclipse, and thus the epoch of its mid-eclipse [4, 6]. Determining the white dwarf's mid-eclipse epoch is much more difficult using observations with poor time resolution for systems with low fluxes, since it becomes impossible to reliably determine the times of the eclipse ingress and egress for the close-binary components; the observed minimum brightness does not necessarily correspond to the mid-eclipse of the white dwarf.

We accordingly used the following procedure to refine the orbital phases of the light curves.

1. We used the ephemeris

$$\begin{aligned} \text{Min. phot.} &= \text{HJD } 2456041.43664 \\ &+ 0.0589106E \end{aligned}$$

to calculate the orbital phases for our observations of April 23, 2012 and to plot the mean light curves. At HJD 2456041.43664, the flux in magnitudes, $V = 20.455^m$, was lowest near the true minimum brightness on the first observing night. Similar ephemerides were derived for each observing night, with the lowest-flux data point near the deepest minimum in the corresponding series used as the initial epoch.

2. When solving for the close-binary parameters based on the shape of the observed light curve, we supplemented the array of unknown parameters with the parameter $\Delta\varphi_I$ (I denoting the number of the light curve; Table 2)—the orbital-phase displacement of the observed light curve relative to the synthetic curve—so that the true epoch of the white dwarf's mid-eclipse would correspond to phase $\varphi = 0.0$.

3. The calculated corrections $\Delta\varphi_I$ were added to the phases of the normal points of the mean light curves (see Table 3 below), the phases of the un-averaged observations, and the epochs of minimum brightness we used. Table 2 contains the “refined”

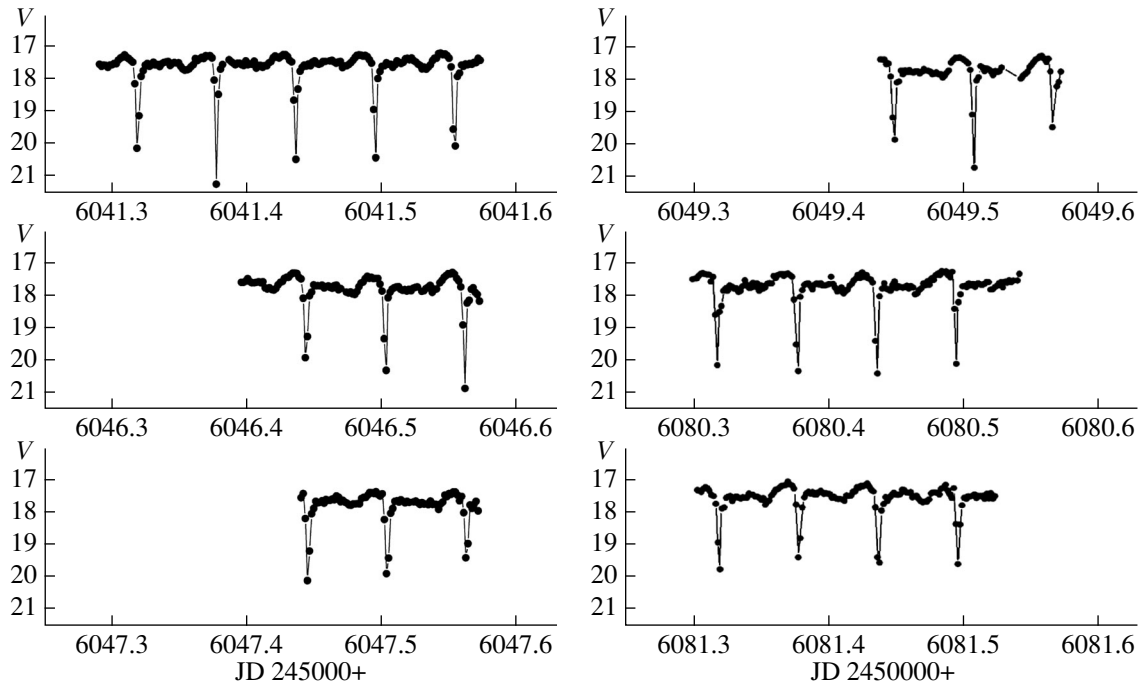


Fig. 3. Unaveraged light curves of J1502 plotted to the same scale for all the nights in April–June 2012.

observed times of the white dwarf’s mid-eclipses obtained in this way. Thus, we used the following ephemeris when computing the orbital phases of our observations:

$$\text{Min. phot.} = \text{HJD } 2456041.4359625(2) \quad (3) \\ + 0.0589106(4)E,$$

where the initial epoch was selected to be the best one for minimizing the $O-C$ values.

5. LIGHT CURVES

Figure 3 displays our V light curves of J1502. Despite some differences in the light-curve shapes, all exhibit deep minima indicating eclipses in the system; the lowest number of minima observed on one night was three, and the highest number five. Figure 3 shows that the minima differ in depth; eclipse depths differ by as much as $\sim 1^m$. The outside-eclipse brightness level also varies, with variations reaching $\sim 0.3^m$. Most of our observations were obtained towards the end of the April outburst, while the observations of June 1 and 2 (i.e., sets 5 and 6) were obtained after the end of the outburst, so that the brightness level here corresponds to quiescence of the system.

Figure 4 shows all our observations of J1502 folded with the orbital ephemeris (2). This figure clearly displays not only the displacement of the minimum relative to phase $\varphi = 0.0$ (Fig. 1), as well as

the large dispersion of the data points for the outside-eclipse orbital phases. This demonstrates that each of the curves should be analyzed separately, rather than analyzing the combined curve only, in order to determine which parameter variations result in the observed large scatter of the data.

Determining the parameters of the system’s components from photometric observations requires reliable light curves that have been cleaned of random flux fluctuations. Our data cover six nights (sets) of observations in 2012. They can be subdivided into two groups separated by slightly more than 400 orbital cycles (Fig. 1, Table 2). The system demonstrated no outburst activity during our observations, but the shape and amplitude of the light curves, and also the brightness at maximum, obviously varied.

The mean light curves we used to determine the parameters of J1502 are presented in Table 3. As a rule, we performed no data averaging within a primary minimum: otherwise, the shape of the minimum would suffer considerable distortion due to the low time resolution and insufficient number of observations at the minima. We estimated the uncertainties of such data points using the mean value of σ calculated for the corresponding light curve outside eclipses. The total number of measurements in the corresponding observing set is given in Table 3 in braces.

Table 3. Mean V light curves of J1502 obtained on April 23, 2012–June 2, 2012

Curve 2 (JD 2456046) {35}				Curve 3 (JD 2456047) {35}				Curve 4 (JD 2456049) {34}			
φ	V	σ	n	φ	V	σ	n	φ	V	σ	n
0.0053	19.893	0.053	1	0.0034	19.864	0.037	1	0.0173	20.709	0.033	1
0.0209	20.835	0.053	1	0.0045	20.076	0.037	1	0.0198	19.843	0.033	1
0.0250	20.283	0.053	1	0.0048	19.377	0.037	1	0.0465	18.093	0.054	3
0.0316	19.240	0.053	1	0.0306	19.161	0.129	3	0.0728	17.997	0.046	3
0.0492	18.118	0.081	2	0.0568	17.922	0.088	3	0.0991	17.665	0.052	3
0.0658	18.049	0.069	2	0.0831	17.852	0.037	3	0.1367	17.709	0.043	4
0.0811	17.872	0.054	2	0.1094	17.667	0.033	3	0.1761	17.688	0.058	2
0.1048	17.729	0.045	3	0.1420	17.649	0.013	4	0.2023	17.672	0.007	2
0.1309	17.716	0.018	3	0.1881	17.627	0.017	4	0.2285	17.744	0.015	2
0.1665	17.781	0.056	5	0.2323	17.652	0.036	3	0.2548	17.805	0.036	2
0.2000	17.792	0.127	4	0.2671	17.618	0.018	2	0.2810	17.719	0.008	2
0.2290	17.691	0.055	4	0.2934	17.636	0.034	2	0.3072	17.732	0.012	2
0.2639	17.616	0.076	4	0.3385	17.602	0.028	3	0.3336	17.759	0.035	2
0.2950	17.683	0.088	3	0.3868	17.567	0.049	4	0.3598	17.670	0.068	2
0.3357	17.708	0.042	6	0.4262	17.693	0.041	2	0.3993	17.670	0.028	2
0.3840	17.672	0.033	5	0.4524	17.638	0.036	2	0.4650	17.752	0.034	3
0.4318	17.679	0.049	5	0.4787	17.694	0.032	2	0.5305	17.781	0.027	2
0.4876	17.741	0.068	4	0.5181	17.726	0.014	4	0.5893	17.864	0.046	3
0.5402	17.791	0.031	6	0.5575	17.695	0.066	2	0.6254	17.890	0.031	2
0.5938	17.819	0.037	6	0.5838	17.724	0.006	2	0.6517	17.834	0.025	2
0.6440	17.820	0.036	5	0.6100	17.721	0.037	2	0.6779	17.751	0.010	2
0.6901	17.615	0.026	5	0.6364	17.722	0.010	2	0.7044	17.644	0.052	2
0.7410	17.483	0.024	6	0.6627	17.797	0.081	2	0.7306	17.488	0.036	2
0.7894	17.369	0.020	5	0.6891	17.631	0.084	2	0.7570	17.404	0.029	2
0.8285	17.371	0.033	4	0.7153	17.585	0.074	2	0.7834	17.333	0.021	2
0.8556	17.270	0.014	2	0.7415	17.481	0.037	2	0.8098	17.320	0.033	2
0.8705	17.363	0.083	2	0.7677	17.463	0.025	2	0.8361	17.303	0.028	3
0.8915	17.377	0.064	2	0.7939	17.380	0.015	2	0.8625	17.312	0.031	3
0.9081	17.367	0.075	2	0.8201	17.393	0.027	2	0.8888	17.346	0.009	3
0.9231	17.427	0.018	2	0.8462	17.369	0.028	2	0.9136	17.458	0.046	2
0.9441	17.572	0.047	2	0.8725	17.343	0.037	2	0.9354	17.430	0.035	4
0.9605	17.584	0.122	2	0.8987	17.434	0.007	2	0.9676	17.762	0.062	3
0.9756	17.948	0.106	2	0.9252	17.537	0.042	3	0.9923	19.110	0.045	2
0.9946	18.878	0.053	1	0.9517	17.428	0.028	3	0.9969	19.452	0.033	1
0.9987	19.301	0.053	1	0.9780	18.112	0.066	3				

Table 3. (Contd.)

Curve 5 (JD 2456080) {48}				Curve 1 (JD 2456041) {37}				Curve 6 (JD 2456081) {34}			
φ	V	σ	n	φ	V	σ	n	φ	V	σ	n
0.0076	20.113	0.020	2	0.0044	20.119	0.030	1	0.0011	19.340	0.034	1
0.0175	20.383	0.046	1	0.0115	20.455	0.030	1	0.0064	19.345	0.034	1
0.0226	20.310	0.046	1	0.0193	20.406	0.030	1	0.0117	19.556	0.034	1
0.0332	18.476	0.046	1	0.0233	20.042	0.030	1	0.0240	19.717	0.034	1
0.0336	18.178	0.046	1	0.0305	19.117	0.030	1	0.0268	19.508	0.034	1
0.0458	18.007	0.007	2	0.0320	18.449	0.030	1	0.0323	18.753	0.034	1
0.0643	18.012	0.146	3	0.0378	18.290	0.030	1	0.0376	18.325	0.034	1
0.0822	17.755	0.041	3	0.0475	17.933	0.032	2	0.0512	17.861	0.035	2
0.1011	17.612	0.026	2	0.0573	17.790	0.111	2	0.0608	17.763	0.031	2
0.1108	17.708	0.037	2	0.0705	17.762	0.016	3	0.0771	17.745	0.049	2
0.1318	17.724	0.045	4	0.0859	17.624	0.058	3	0.0916	17.493	0.054	3
0.1575	17.662	0.047	4	0.1066	17.558	0.009	4	0.1204	17.456	0.044	6
0.1834	17.714	0.037	4	0.1402	17.539	0.020	6	0.1595	17.464	0.031	6
0.2077	17.684	0.054	3	0.1799	17.514	0.024	8	0.1980	17.392	0.026	6
0.2307	17.657	0.049	4	0.2274	17.506	0.018	10	0.2370	17.438	0.022	6
0.2532	17.694	0.050	3	0.2800	17.504	0.015	10	0.2755	17.390	0.036	6
0.2791	17.694	0.060	4	0.3327	17.472	0.020	10	0.3193	17.388	0.039	7
0.3055	17.689	0.053	4	0.3809	17.427	0.015	6	0.3628	17.406	0.036	6
0.3306	17.660	0.012	3	0.4311	17.466	0.032	7	0.4009	17.384	0.030	6
0.3479	17.631	0.068	3	0.4817	17.437	0.020	8	0.4404	17.455	0.028	6
0.3656	17.650	0.026	3	0.5314	17.514	0.023	8	0.4786	17.461	0.013	6
0.3852	17.617	0.035	3	0.5786	17.585	0.022	10	0.5272	17.543	0.014	6
0.4090	17.665	0.047	4	0.6286	17.607	0.020	9	0.5789	17.602	0.030	6
0.4348	17.646	0.090	4	0.6787	17.556	0.025	10	0.6309	17.539	0.036	6
0.4606	17.673	0.048	4	0.7284	17.428	0.033	9	0.6828	17.363	0.022	6
0.4866	17.767	0.056	4	0.7786	17.339	0.014	10	0.7325	17.255	0.023	6
0.5124	17.759	0.073	4	0.8313	17.260	0.017	10	0.7715	17.284	0.035	6
0.5386	17.752	0.054	4	0.8735	17.260	0.013	6	0.8101	17.151	0.019	6
0.5645	17.673	0.043	4	0.8995	17.281	0.030	4	0.8491	17.137	0.019	6
0.5904	17.746	0.065	4	0.9194	17.317	0.044	3	0.8878	17.132	0.050	6
0.6162	17.687	0.062	4	0.9330	17.353	0.043	3	0.9268	17.351	0.059	6
0.6421	17.621	0.057	4	0.9501	17.374	0.041	3	0.9653	17.482	0.112	6
0.6716	17.595	0.027	5	0.9653	17.515	0.046	3	0.9856	18.312	0.034	1
0.6995	17.485	0.042	5	0.9789	18.075	0.058	2	0.9983	18.888	0.034	1
0.7220	17.484	0.013	4	0.9851	18.630	0.030	1				
0.7455	17.410	0.025	4	0.9930	18.919	0.030	1				
0.7718	17.364	0.037	5	0.9972	19.527	0.030	1				
0.7979	17.333	0.025	5								
0.8232	17.255	0.020	4								
0.8493	17.324	0.031	4								
0.8754	17.289	0.025	4								
0.9012	17.348	0.035	4								
0.9270	17.433	0.045	4								
0.9530	17.395	0.069	4								
0.9709	18.093	0.046	1								
0.9819	18.475	0.096	2								
0.9916	19.372	0.046	1								
0.9968	19.487	0.046	1								

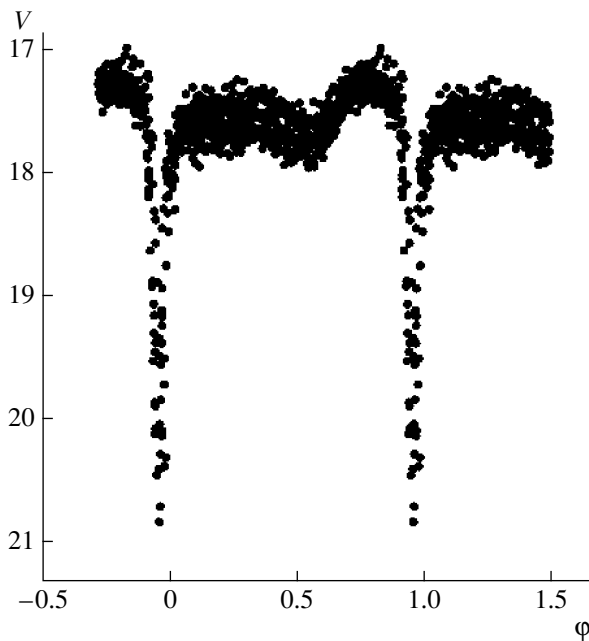


Fig. 4. All V observations of J1502 obtained in 2012, folded.

6. THE CLOSE-BINARY MODEL USED TO DETERMINE THE CLOSE-BINARY PARAMETERS

It follows from gas-dynamical studies of steady-state matter flows in semi-detached binary systems that the interaction between the stream and the disk is collisionless [9–14]. The interaction between the stream and the gas in the circum-disk halo forms an extended region of enhanced energy release, sometimes called a “hot line.” This is a fundamental difference from the generally accepted “hot-spot” model, which supposes that the stream collides with the lateral surface of the accretion disk. The main features of the morphology of matter flows in semi-detached binaries with stationary “cool” disks ($T_{\text{eff}} \sim 10\,000\text{--}15\,000\text{ K}$) are described in [12, 15].

The gas-dynamical computations [12] demonstrate that the interaction between the circum-disk halo and the stream in the case of a cool disk exhibits all the characteristic signatures of an oblique collision of two flows, forming a structure consisting of two shocks and a tangential discontinuity between them. The structure of the region of collisional interaction between the stream and the halo is complex. Parts of the halo that are far from the disk have low density, and the shock due to their interaction with the stream is located along the edge of the stream. The extent of this structure is fairly large; this component of the region of energy release is similar to the hot line obtained earlier in computations for a “hot” accretion disk, but it does not coincide with the tangent to the lateral surface in the cool-disk case. With increasing

halo gas density, the shock becomes curved and, as a result, assumes a position on the lateral disk surface, on the leeward side of the stream. At the interaction site, the halo gas and stream gas pass through the shocks corresponding to their flows and become mixed, and this matter moves along the tangential discontinuity between the two shocks and heats matter on the leeward side of the disk: an analog of a classical hot spot.

In the model used, which is based on the gas-dynamical computations [12], the region of energy release includes two regions on the surface of the hot line, on its windward and leeward sides near the disk, and a hot region on the disk’s lateral surface, represented by a half-ellipse on the leeward side of the line, with the center coincident with the intersection of the axis of the gas stream—the hot line—with the disk. This “combined” model is described in detail in [16]. This structure of the energy-release region has fundamental differences compared to the generally accepted model of cataclysmic variables, which supposes that the center of the hot spot lies at the intersection of the ballistic trajectory of the gas stream flowing from the secondary and the matter of the lateral surface of the disk.

The jump of the gas parameters after its passage through the shocks also results in an increase in the pressure in the region between the shocks and, as a consequence, to the appearance of a pressure gradient perpendicular to the orbital plane of the system. Hence the gas begins to expand, moving away from the orbital plane until the gas-pressure gradient

becomes equal to the gravitational force. This motion of gas, together with its motion along the tangential discontinuity along the outer edge of the disk, gradually increases the thickness of the circum-disk halo, so that the region of acceleration is mainly confined to the region of interaction between the disk and the stream. For this reason, the model used assumes that the thickness of the disk's outer edge is largest in the region of the collision between the stream and the disk, and gradually decreases to its unperturbed state on the leeward side of the stream. The entire region of the disk where the thickness of its outer edge exceeds the thickness of the unperturbed disk corresponds to the hot-spot region.

A schematic view of the system components in the combined model for various orbital phases is shown in Fig. 5. The regions of enhanced energy release near the disk edge (A) and the cooler body of the gas stream located outside the shock-heated region (B) are marked on the surface of the hot line. The arrows indicate the increased thickness of the disk edge in the hot-spot region, resulting in the deformation of the corresponding inner parts of the disk.

Let us consider the main features of this model. We present a brief description of the main characteristics of the combined model used and the parameters of the model below. More complete information can be found in [16].

1. The close binary components are:

- the late-type star with a non-spherical shape;
- the white dwarf;
- the accretion disk with a complex shape surrounding the white dwarf;
- the gas stream;
- the region of interaction between the gas stream and disk, represented by the base of the hot line and the hot spot.

When studying cataclysmic variables, it is traditional to call the white dwarf the primary and the late-type star the secondary. All sizes in the model are expressed in units of the component separation a_0 , with $a_0 = 1$.

2. The shape of the secondary (red dwarf) was specified by a Roche potential with filling factor $\mu = 1.0$. The surface of the star was subdivided into 648 area elements, for each of which the intensity of the radiation emerging towards the observer was computed, with gravitational darkening and limb darkening taken into account (we used a non-linear limb-darkening law).

3. We described the surface of the primary as a sphere with the radius R_{wd} ; the intensity of its light was specified using the effective temperature T_{wd} via a Planck distribution.

4. The white dwarf was surrounded by an opaque, slightly elliptical ($e < 0.2$) accretion disk with a complex shape (see [17] for details); the star's center was located at one focus of the disk's ellipsoid. The disk's shape and radiation intensity were described using the following parameters.

The unperturbed disk was represented with a figure formed by the intersection of the ellipsoid abc of the disk with semi-axes a , b , and c and two paraboloids defined with the parameter A . Together with the semi-axis a , they determine the thickness of the disk's outer edge, β_d . The ellipsoid abc determines the shape of the outer (lateral) surface of the disk. The paraboloids define the shape of the inner surfaces of the elliptical disk (upper, $z \geq 0$, and lower, $z < 0$, relative to the orbital plane).

Another parameter defining the disk shape is the eccentricity of the ellipsoid abc in the orbital plane; we assumed $e < 0.1$.

The alignment of the elliptical disk is given by the angle α_e between the radius vector from the center of the white dwarf to the periastron point of the disk and the line joining the component centers. The disk temperature varies radially according to the relation

$$T(r) = T_{in} \left(\frac{R_{in}}{r} \right)^{\alpha_g}, \quad (4)$$

where T_{in} is the temperature in the inner parts of the disk, near the star's equator, at the distance $R_{in} \sim R_{wd}$ from its center. It is usually assumed that, in a first approximation, if each point of the disk surface radiates as a blackbody, the parameter α_g has its canonical value, $\alpha_g = 0.75$ [18]. During outbursts of cataclysmic variables, when the flux from the disk increases by a large factor, α_g can decrease to ~ 0.1 , resulting in a flatter radial temperature distribution and a higher flux from the accretion disk.

When computing the local temperature of an area element on the disk, we took into account heating by radiation from the secondary (this effect is usually insignificant) and the high-temperature radiation coming from inner parts of the disk. The latter effect also increases the temperature of the matter on the side of the secondary that faces its companion (the reflection effect).

5. The optically opaque part of the gas stream, the hot line (Fig. 5), is represented with a figure that is part of the ellipsoid $a_v b_v c_v$ whose major axis b_v coincides with the axis of the gas stream flowing from the inner Lagrange point L_1 and whose center is located inside the body of the disk, in the orbital plane. We assumed that $b_v \gg a_v$ and $b_v \gg c_v$; i.e., the hot-line ellipsoid is fairly elongated, so that its leeward part forms a blunt angle with the disk surface. Only the part of this ellipsoid situated outside the

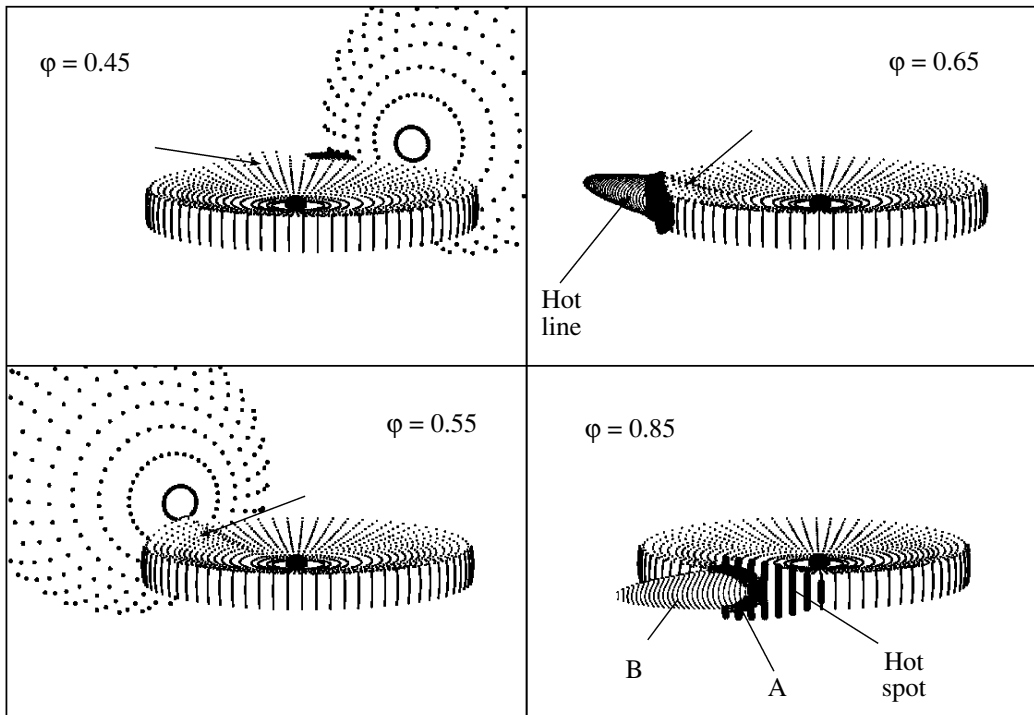


Fig. 5. Schematic view of the system components in the combined model at various orbital phases.

accretion disk is used was the hot line. The parts of the hot line closest to the disk (region A in Fig. 5) have higher temperatures than neighboring parts at larger distances from the disk, due to the collisional interaction between the flows arriving at the disk and the matter of the gas stream.

The energy of the shock is released at the surface of the hot line in accordance with a Planck distribution, both on the side of the arriving stream (the “windward” side) and the opposite (“leeward”) side. We computed the temperatures of area elements on the surface of the hot line independently for both its sides. This temperature varies according to a cosine law, with the maximum values $\Delta T_{ww,max}$ and $\Delta T_{lw,max}$ on the windward and leeward sides. $\Delta T_{ww,max}$ and $\Delta T_{lw,max}$ are parameters of the problem. When computing the resulting gas temperature in the region of energy release near the disk, they are added to the temperature the matter in these regions would have in the absence of the shock.

6. To model the region of interaction between the disk and the stream (the perturbed disk) on its leeward side, we assumed the presence on the lateral surface of the disk at this location of a region with a complex shape and a temperature higher than in the adjacent regions: a hot spot. The thickness z of the disk’s outer edge in the region of the hot spot can be greater than or equal to the thickness of the unperturbed disk (z_{cr}). Formulas that can be used

to compute z_{cr} are presented in [16, 17]. When the thickness of the disk edge in the region of the hot spot c_{sp} is larger than z_{cr} , it is described with the parameter k_{sp} , $c_{sp} = k_{sp}z_{max}$. Here z_{max} is the z coordinate of the intersection of the hot-line ellipsoid with the lateral surface of the disk, and is computed in the process of finding the shapes of the disk and hot spot.

The hot-spot half-ellipse is largest in the orbital plane. For the hot-spot half-ellipse located on the leeward side of the gas stream, the radius of the spot in the orbital plane (R_{sp}) is the sum of the semi-axis of the part of the hot-line ellipsoid that intersects the disk surface (x_{lw}) and the radius of the part of the hot spot that is not covered by the body of the hot line (a_{sp}), $R_{sp} = x_{lw} + a_{sp}$. If R_{sp} is specified in advance in the search for the component parameters, a situation can arise when a_{lw} is smaller than x_{lw} , since x_{lw} and R_{sp} are independent from each other and initially unknown. When $a_{sp} = 0$ (i.e., $R_{sp} = x_{lw}$), there is no hot spot. a_{sp} is a model parameter. There is no hot spot on the windward side of the gas stream.

The local temperature at point j on the disk inside the hot spot varies according to a cosine law:

$$T_j = T_d + T_U \cos\left(\frac{\pi r_j}{2R_{sp}}\right), \quad (5)$$

where T_U is the temperature of the matter at the point U of the intersection between the hot-line axis and the disk; it is not specified explicitly, but is computed in the process of finding the synthetic light curve using (5), such that the temperature T_j at the point of intersection of the hot-line ellipsoid with the disk surface in the orbital plane obtained using (5) is equal to $\Delta T_{lw,\max}$. This approach makes it possible to reduce the number of unknown parameters. Here, r_j is the length of the radius vector from the point U to the center of the j th area element. If the point j is not in the region of the hot spot, its temperature remains the same (T_d) and is determined only by the distance from the compact object and the amount of heating by the components' radiation.

Thus, formally, the desired parameters in the model used are the

- (1) component-mass ratio $q = M_{wd}/M_{\text{red}}$;
- (2) orbital inclination i ;
- (3–4) effective temperatures of the white dwarf T_{wd} and the red donor star T_{red} ;
- (5) radius of the white dwarf R_{wd} ;
- (6) temperature in the inner regions of the disk (or in the boundary layer) near the equator of the white dwarf T_{in} ;
- (7)–(11) parameters of the slightly elliptical disk: the eccentricity e ($e < 0.1$), semi-major axis a , parameter α_g describing the character of the radial temperature variations in accordance with (4), azimuth of the disk's periastron α_e , and thickness of the disk's outer edge $\beta_d = f(A, a)$;
- (12)–(17) parameters of the hot line: the ellipsoid semi-axes a_v, b_v, c_v , maximum temperatures of matter heated with the shock energy on the surface of the line near the disk's outer boundary to the windward $\Delta T_{ww,\max}$ and leeward $\Delta T_{lw,\max}$ sides; these temperatures were added to the temperature $T_d(j)$ the matter would have at the given distance from the disk center $r(j)$ in the absence of a shock:

$$T(j) = T_d(j) + \Delta T_{n,\max} \cos \delta r, \quad (6)$$

where $n = ww$ or lw ; δr is the displacement along the axis of the hot line, computed in the course of the solution.

Since the total number of parameters is 17 (the actual number of variables is 22, including the displacement $\Delta\varphi$ described in Section 4; however, some are technical quantities with very narrow ranges of variation; variations of these parameters within pre-defined ranges have little influence on the synthetic light curves compared to the influence from the main parameters), it is necessary to take into account additional information on the system in order to fix some parameters during the solution and significantly reduce the variation ranges for the others.

The light curves of J1502 we used to determine the parameter values form a homogeneous set of light curves obtained using the same instrument and the same comparison star. This makes it possible to impose an additional constraint on the range of permitted parameter values. Namely, the fluxes for a sequence of several of our synthetic light curves were converted into magnitudes using the same energy unit—the flux from the system at an orbital phase near quadrature for the curve with the lowest outside-eclipse brightness. This enabled us to use both the light-curve shape and the flux variations when comparing the synthetic and observed light curves. A detailed description of this technique can be found in many of our papers (e.g., [19]).

We solved for the system parameters that provided a synthetic light curve that best fit the observed light curve using the Nelder–Mead method [20], which is also described in [21]. When searching for the global minimum of the residuals, we used several dozen different initial approximations for each light curve: since the number of independent variables is large, there typically exists a number of local minima in the studied parameter range. We estimated the goodness of fit between the theoretical and observed light curves of the close binary in the model used by calculating the residuals

$$\chi^2 = \sum_{j=1}^N \frac{(m_j^{\text{theor}} - m_j^{\text{obs}})^2}{\sigma_j^2}, \quad (7)$$

where m_j^{theor} and m_j^{obs} are the object's magnitudes at the j th orbital phase from the theoretical model and observations; σ_j^2 is the dispersion of the observations for the j th data point and N is the number of normal points in the curve.

7. RESULTS OF LIGHT-CURVE MODELING FOR J1502

We solved for the best-fit system parameters for a sequence of uniform light curves using the combined model in two stages.

In the first, we determined the scaling radiation flux, F_0 , needed to translate the theoretical F values into magnitudes, and $V(0)$ corresponding to this flux. Usually, when normalizing a sequence of uniform light curves, the search for F_0 makes use only of the curve with the lowest out-of-eclipse flux. However, in the case of J1502, the out-of-eclipse flux is approximately the same for all six curves. For this reason, in the first stage, we searched for the parameters without reduction to a standard radiation flux, using each of the six light curves independently. The parameters q , i , T_{wd} , and R_{wd} were restricted to the ranges $q = 8.8\text{--}9.2$, $i = 87.8^\circ\text{--}88.6^\circ$, $T_{\text{red}} = 2000\text{--}3000$ K,

$e = 0.001-0.1$, $R_d(\text{max})/\xi = 0.35-0.65$, $R_{wd}/\xi = 0.0273-0.0290$ (ξ is the distance between the white dwarf's center of mass and the inner Lagrange point L_1 ; for the selected mass ratio range, $\xi/a_0 = 0.7081-0.7108$); $T_{wd} = 10\,600-13\,000$ K according to [5] (Table 1). We selected a radiation flux satisfying all the curves from among the obtained sets of solutions: namely, we assumed that the radiation flux $F_0 = 0.870994$ conditional units corresponds to the magnitude $V(0) = 17.37^m$. Our use of conditional units is due to the fact that the Planck function applied to compute the radiation flux from area elements in a unit wavelength interval (in our case, in centimeters) is the energy flux passing through a 1 cm^2 area. The distance unit in the program code is the component separation a_0 , which is not known in advance.

In the second stage, we searched for the best-fit parameters of J1502 for all six light curves, normalizing the radiation fluxes to F_0 . To reduce the total number of unknown parameters, we fixed the following values: $q = 8.94$, $i = 88.0^\circ$, $T_{\text{red}} = 2650$ K, $R_{wd}/\xi = 0.0279$, $T_{wd} = 11\,720$ K, which are close to those presented in Table 1, taking into consideration their uncertainties. These values are the results of averaging the corresponding parameters derived in the first stage for the six light curves. Further, we performed a new search for the system parameters. The results are collected in Table 4.

We estimated the uncertainties of the computed parameters as follows. Due to the very small uncertainties of the mean data points, for none of the obtained solutions of the J1502 light curves were we able to obtain a residual below the critical significance level $\chi_{0.001,N}^2$ (the critical significance level for $\alpha = 0.001$ and the number of degrees of freedom $N = 34-48$, for different light curves, is $\chi_{0.001,N}^2 = 65.5-85$). We can estimate the influence of changes of a parameter on the solution if we specify a conditional uncertainty limit instead of the critical value, for example, by increasing the value of the minimal residual we obtained for a specified light curve by 10%, $1.1\chi_{\text{min}}^2$. We then varied the selected parameter until the fit reached the residual $1.1\chi_{\text{min}}^2$, with the remaining parameters fixed at the values that provided the minimum residual. The resulting uncertainties for the one to two last digits of the parameter are given in parentheses.

Table 4 also presents several values derived from one or several parameters that demonstrate the system's characteristics more visually. For example, the temperature T_U is a function of the hot-spot size, disk radius, the temperature of matter heated by the shock on the leeward side of the hot line, etc., while β_d depends on the disk radius and, in a complex

way, the parameter A (the parameter A was used when estimating the thickness of the disk's outer edge z_{cr} [22]). The uncertainties of such "dependent" parameters were determined using the uncertainty of the "independent" parameter that had the largest influence on the value in question.

Finally, we estimated how the obtained solutions were influenced by variations of the parameters that had been fixed. As expected, the solution is least sensitive to changes in the component-mass ratio q , with the uncertainty reaching 7%, $q = 8.94 \pm 0.65$. The uncertainties of the parameters that depend on q —the mean radius of the secondary and the distance between L_1 and the white-dwarf center of mass—are less than 2.5% and 1%, respectively: $\langle R_{\text{red}} \rangle = (0.2202 \pm 0.0053)a_0$, $\xi = (0.7085 \pm 0.0068)a_0$. The solutions obtained are also quite sensitive to changes in the stellar temperatures and the radius of the white dwarf, which are 1.5–2.5%: $T_{\text{red}} = 2650 \pm 65$ K, $T_{wd} = 11720 \pm 160$ K, $R_{wd} = (0.0279 \pm 0.0005)\xi = (0.0198 \pm 0.0003)a_0$. The solution is most sensitive to the orbital inclination: $i = 88.0^\circ \pm 0.1^\circ$.

Figure 6 presents theoretical light curves for the corresponding parameters. The observed light curves of J1502 in quiescence can be reproduced successfully, enabling firm conclusions about variations of the disk parameters during variations in the system's brightness in the model used. The quality of the fit of the light curves near the primary minimum is shown visually in Fig. 7. To the left in each panel we show the unaveraged light curves along with the synthetic light curve for the parameters of Table 4 for the corresponding date; to the right, we display the parts of the corresponding light curve in the region of the primary minimum ($\varphi \sim 0.8-1.2$), with a smaller orbital phase increment. Some of the light curves reveal a small step at orbital phases $\varphi \sim 0.05-0.1$, due to the egress from the eclipse of the windward side of the hot line, as follows from a consideration of the orbital variations of the components' contributions to the combined brightness of the system.

Figure 8 shows the contributions of the system's components to the combined flux from the system in conditional units for sets 1–6 (numbers at the top of the panels): the (1) red and (2) white dwarfs, (3) disk with the hot spot, and (4) hot line. Table 5 presents the flux variation limits for the corresponding components, to facilitate comparison of these contributions for different datasets.

The following conclusions can be drawn from an analysis of Fig. 8 and Table 5.

1. The light-curve amplitudes of J1502 in quiescence are mainly determined by the orbital variability of the white dwarf. The out-of-eclipse flux from the donor star in panels 4 and 5 is constant, at the

Table 4. Parameters of J1502 in 2012 determined for the combined model

Parameter	JD 2456041	JD 2456046	JD 2456047	JD 2456049	JD 2456080	JD 2456081
$q = M_{wd}/M_{red}$	8.94 (fixed)					
i , deg	88.0 (fixed)					
$\langle R_{red} \rangle$, a_0	0.2202 (fixed)					
T_{red} , K	2650 (fixed)					
ξ , a_0	0.7085 (fixed)					
R_{wd}	0.0279 $\xi = 0.0198a_0$ (fixed)					
T_{wd} , K	11720 (fixed)					
ΔV	3.20 ^m	3.57 ^m	2.74 ^m	3.41 ^m	3.13 ^m	2.59 ^m
Accretion disk						
e	0.017(7)	0.013(7)	0.016(6)	0.009(7)	0.023(9)	0.013(7)
R_d , ξ	0.613(9)	0.583(8)	0.563(9)	0.560(15)	0.577(15)	0.588(10)
a , a_0	0.427(7)	0.408(6)	0.393(7)	0.393(11)	0.399(10)	0.411(8)
$0.5\beta_d$, °	2.2(1)	2.2(2)	2.2(3)	2.4(1)	2.5(1)	2.2(1)
α_e , °	78(2)	82(2)	73(2)	89(2)	74(2)	74(1)
α_g	0.696(15)	0.74(1)	0.654(13)	0.652(23)	0.623(21)	0.592(12)
$\langle T_{in} \rangle$, K	20260(580)	15575(1100)	16115(450)	15560(800)	17100(845)	17680(510)
$\langle T_{out} \rangle$, K	2530(65)	1955(100)	2425(60)	2415(105)	2795(125)	3015(80)
Hot spot						
R_{sp} , a_0	0.156(17)	0.262(25)	0.156(22)	0.170(35)	0.184(33)	0.139(20)
T_U , K	6740(440)	6340(350)	6155(380)	7065(515)	5850(560)	5820(660)
$0.5z_{sp}$, deg	2.3(2)	3.0(3)	2.7(6)	2.7(4)	3.2(6)	2.5(3)
Hot line						
a_v , a_0	0.067(3)	0.091(4)	0.048(7)	0.074(4)	0.070(6)	0.036(3)
b_v , a_0	0.330(7)	0.347(9)	0.367(11)	0.334(14)	0.392(23)	0.313(18)
c_v , a_0	0.020(2)	0.021(2)	0.019(2)	0.019(3)	0.020(2)	0.019(3)
$T_{ww,max}$, K	7650(1600)	7280(1500)	7370(1360)	7265(960)	7325(2200)	7710(2000)
$T_{lw,max}$, K	7510(140)	7125(105)	7185(130)	7160(270)	7260(200)	7575(250)
β_1 , °	22(1)	19(1)	24(1)	21(1)	20(1)	28(1)
χ^2	755	340	524	965	1060	1052

$\Delta V = \langle V_{min} \rangle - \langle V_{max} \rangle$ is the amplitude of the mean light curve; R_d/ξ the disk radius at apoastron in units of the distance ξ between the white dwarf's center of mass and the inner Lagrange point L_1 ; $0.5\beta_d$ the half-thickness of the disk's outer edge, which depends on the parameters A and a/a_0 (see item 4 in Section 6); a/a_0 the semi-major axis of the elliptical disk; $\langle T_{in} \rangle$, $\langle T_{out} \rangle$ the mean temperatures in inner regions of the disk (in the boundary layer) and at its outer edge; R_{sp}/a_0 the radius of the hot spot on the disk's lateral surface, to the leeward side of the stream; T_U the temperature on the axis of the stream, at the point U where it intersects the lateral surface of the disk, approximated from $T_{lw,max}$, as computed during the solution; $0.5z_{sp}$ the half-thickness of the hot spot, which depends on k_{sp} and z_{max} , computed in the solution; a_v , b_v , c_v the half-axes of the ellipsoid, with the center inside the disk and the part of the ellipsoid outside the disk determining the shape of the hot line, presented to give an idea of the elongation of the hot line's truncated ellipsoid; $T_{ww,max}$ (and $T_{lw,max}$) the sum of $\Delta T_{ww,max}$ (or $\Delta T_{lw,max}$) and the temperature of matter near the disk, on the corresponding side of the stream in the absence of the shock [see (6)]; β_1 the angle formed by the axis of the stream with the line connecting the centers of mass of the components.

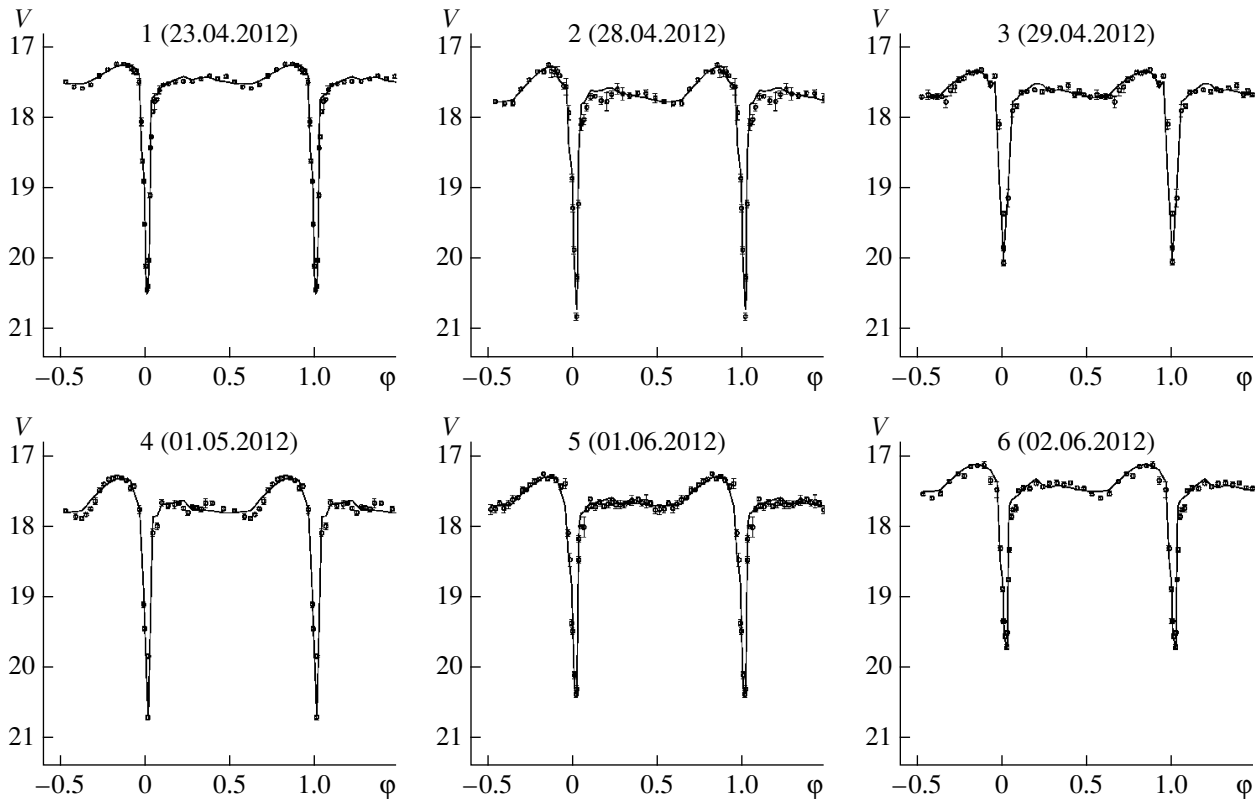


Fig. 6. The mean light curves of J1502 obtained in 2012 (points) compared to theoretical curves synthesized with the parameters from Table 4 (solid curves). The vertical bars indicate the rms uncertainties of the data points on the mean curves.

level of 0.49 conditional units. This radiation flux level is observed in the other sets only at phases $\varphi \sim 0.5-0.9$, while the flux increases to 0.59 conditional units at phases just after the eclipse, $\varphi \sim 0.1-0.5$, for a constant temperature of the primary during all six sets of observations.

Let us consider possible origins of this effect.

A check of the visibility conditions for areas on the surface of the white dwarf shows that, at orbital phases $\varphi \sim 0.2-0.3$, the number of area elements on the surface of the primary that are not screened by the disk edge is 7–8% larger in sets 1–3 and 6 than in sets 4 and 5. These additional area elements are near the orbital plane, so that their visibility conditions are most favorable for the observer, increasing the combined radiation flux from the primary by 15–17%. The alignment of the elliptical disk is such that, near phases $\varphi \sim 0.2-0.3$, the distance from the disk edge to the white dwarf is the largest for the observer and the disk’s apoastron lies on the line between the observer and the primary, so that, even small variations of the disk radius and the thickness of its outer edge can change the number of area elements on the star visible to the observer at these phases. This effect is discussed in detail in [17, Fig. 4]. This conclusion is supported by Table 4: the half-thickness of the

disk’s outer edge is $\sim 8\%$ larger during sets 4 and 5 than in the other sets— $\beta_d \sim 2.4^\circ-2.5^\circ$ as opposed to $\sim 2.2^\circ$ —and the disk radius in those two sets was smaller than during sets 1–3 and 6 (with one exception).

2. The orbital variations of the flux F_{red} from the donor indicate that the ellipsoidal effect is dominant in giving rise to the variability. With the exception of sets 1, the reflection effect has little influence; it is manifest only as a slight increase in the radiation flux at the quadratures and at the secondary minimum (phase $\varphi \sim 0.5$) (Table 5). In the model considered, this is due to the higher temperature of the disk’s inner regions during the first sets, compared to the temperature T_{in} in the other sets ($T_{\text{in}} > 20\,000$ K versus $15\,000-17\,000$ K).

3. While the radiation flux from the white dwarf determines the orbital variability amplitude of J1502, the details of its out-of-eclipse brightness are determined by the flux from the disk, with the hot spot on its lateral surface (curves 3 in Fig. 8). No total eclipse of the disk is observed for any of the light curves (Table 5). It follows from Table 4 that the disk radius (R_d/a_0) is always a factor of 1.5–2 larger than the mean radius of the red dwarf, and even the smallest radius is a factor of 1.4 larger than the radius determined in [5] for

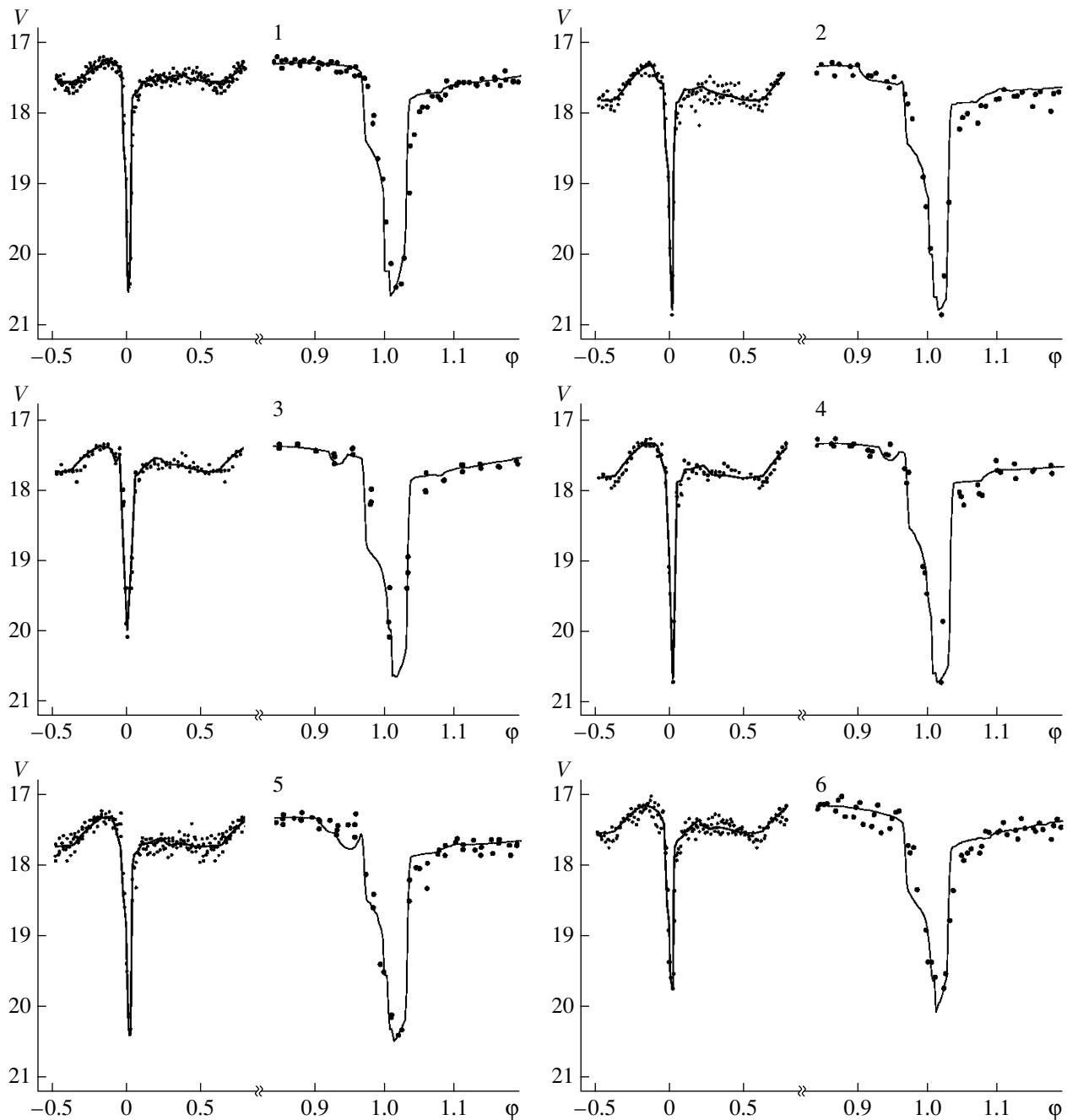


Fig. 7. Unaveraged light curves of J1502 obtained in 2012 (points), compared to theoretical curves synthesized with the parameters from Table 4 (solid curves). The left curve shows the orbital curves and the right curve the observations around the primary minimum ($\varphi \sim 0.8-1.2$).

quiescence ($R_d \sim 0.28a_0$; Table 1). The disk radius derived from the data for sets 1 (April 23, 2012), which is closest in time to the outburst, is $R_{d,1} \sim 0.61a_0$, while the radii found for the other sets are smaller, and vary within 4–9% of $R_{d,1}$. The radiation flux from the accretion disk at orbital phases $\varphi \sim 0.1-0.6$, which approximately coincide with a plateau in the radiation curves for the disk, shows a weak dependence on

the disk radius or the parameter α_g for the radial temperature distribution. The radiation flux in the light curve near the plateau is higher in set 6 (June 2, 2012) than in the other sets (by factors from 3 to 20); the disk radius is the second largest, and α_g is the lowest.

The orbital hump in the light curves is due to the combined contribution of light from the hot spot

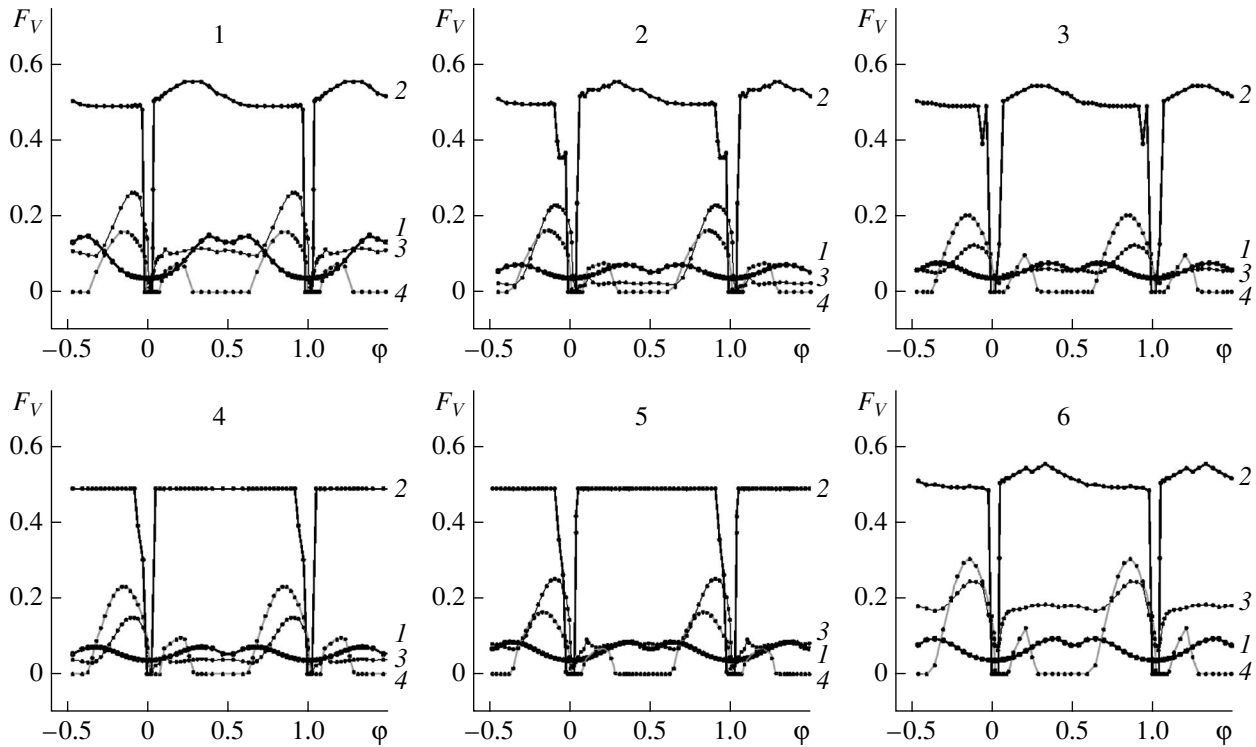


Fig. 8. Contributions of light from the components of J1502 to the combined quiescent flux in 2012 (in conditional units). Shown are the contributions from the red dwarf (1), white dwarf (2), accretion disk with the bright spot on its lateral surface (3), hot line (4). The numbers at the top of the panels correspond to the number identifying the observation set.

on the disk’s surface, light from the leeward side of the hot line, and the disk temperature at its outer edge, while the radiation flux from the hot spot is proportional to the product of the spot’s size ($\sim R_{sp}$) and its temperature ($\sim T_U$).

4. The light from the hot spot (mainly from regions adjacent to the lateral surface of the disk) contributes to the combined flux from the system in two sections of the orbital curves, with maxima at orbital phases $\varphi \sim 0.2$ and 0.8 , due to the windward and leeward sides of the stream, respectively, entering the line of sight. It follows from Table 4 that the resulting temperatures of the matter here ($T_{ww,max}$ and $T_{lw,max}$) differ only insignificantly; since the visibility of the shock region is more favorable on the leeward side of the stream than on its windward side, the flux from the former region is more than twice the flux from the latter region. The presence of flux from the stream at $\varphi \sim 0.2$ creates a small hump in the light curve at the egress from the eclipse; in the absence of this contribution, the flux from the system here would have been at the level of the secondary minimum at phases $\varphi \sim 0.5-0.6$. The flux from the stream at $\varphi \sim 0.8$ is added to the radiation from the hot spot, increasing the orbital hump at the eclipse ingress.

8. DISCUSSION

Our observations were obtained 300–350 orbital cycles after the end of the system’s outburst in April. At that time, the flux from the system was close to that observed during its quiescence. However, our model computations demonstrate that the disk radius was still fairly large during our observations, smoothly decreasing from $R_d \sim 0.613a_0$ to $\sim 0.560a_0$ during orbital cycles $I = 0-137$ (Table 2), and then increasing to $R_d/a_0 \sim 0.577-0.588$ in orbital cycles 662–677. Similar changes are demonstrated by the temperature in the inner regions of the disk: in the first group ($I = 1-137$), the temperature $\langle T_{in} \rangle$ decreased from $\sim 20\,000$ K in the first set to $\sim 15\,000$ K in sets 4, and it increased in the second group ($I = 662-677$) ($\langle T_{in} \rangle \sim 17\,000$ K and $18\,000$ K).

The radial temperature distribution specified by α_g also varies. In the first group, it is close to the stationary value, $\alpha_g \sim 0.65-0.75$. In the second group, the radial temperature distribution is flatter, and α_g decrease: $\alpha_g \sim 0.62$ and ~ 0.59 for sets 5 and 6, respectively. As was noted above, we observed the highest out-of-eclipse radiation flux from the disk in set 6; the out-of-eclipse flux from the disk increased by a factor of 2.5 within 15 orbital cycles between sets 5 and 6 (the second group of observations).

Table 5. J1502 component fluxes in conditional units for 2012, determined from the solution for the system parameters in the combined model

Parameter	JD 2456041	JD 2456046	JD 2456047	JD 2456049	JD 2456080	JD 2456081
Donor star						
Minimum $\varphi = 0.0$	0.037	0.037	0.037	0.037	0.037	0.037
Minimum $\varphi = 0.5$	0.132	0.053	0.058	0.053	0.067	0.077
Quadratures	0.151	0.073	0.077	0.072	0.085	0.094
White dwarf						
Minimum $\varphi = 0.0$	0.0	0.0	0.0	0.0	0.0	0.0
Maximum	0.558	0.558	0.547	0.492	0.492	0.558
Accretion disk						
Minimum $\varphi = 0.0$	0.011	0.0023	0.024	0.005	0.018	0.063
(Plateau $\varphi \sim 0.1-0.6$)	0.10	0.024	0.058	0.036	0.072	0.18
Orbital hump	0.263	0.230	0.125	0.149	0.253	0.245
Hot line						
Minimum $\varphi = 0.0$	0.0	0.0	0.0	0.0	0.0	0.0
Maximum $\varphi \sim 0.2$	0.075	0.076	0.098	0.096	0.076	0.122
Maximum $\varphi \sim 0.8$	0.160	0.164	0.204	0.232	0.164	0.305

Since a decrease in α_g is usually related to decreasing viscosity of the matter in the disk, this suggests the presence of oscillatory processes in the body of the disk between outbursts.

Theoretically, oscillatory processes in the disk could be due to a non-circular shape of the accretion disk, since an elliptical disk will inevitably precess due to the tidal influence of the secondary and, as a consequence, the gas density, gas velocity, and the energy released at the shock front in the region where the flows in the disk interact with the gas stream will vary for different orbital cycles. However, the disk eccentricities found from the solution for all six light curves are very small, $e \sim 0.01-0.02$ (Table 4), and the ratio of the disk semi-axes in this case is $b/a \sim 0.99995-0.9998$, so that the disk is essentially circular. The alignment of the disk, as reflected by α_e , does not show any regular variations in the first group and is constant in the second group. Hence, if the disk as a whole is precessing, this effect is very small.

The considerable accumulation of matter in the disk, indirectly indicated by the growth of its radius in the second group of observations, could result in the formation of a precession-type density wave [23] in its inner regions, which have higher densities than the outer parts. However, in the model used, we did not consider the presence of such a wave in the inner disk due to the a complex relationship between α_g

and the coordinates of an area element's center on the disk, increasing the number of unknown variable parameters. In the model used, oscillatory processes in the disk are most likely due to instabilities in the matter outflow from the secondary and the related non-uniform character of matter input into the disk.

We can judge the intensity of the matter outflow from the red dwarf using the parameter β_1 , which is the angle between the axis of the gas stream and the line joining the centers of mass of the stars. The larger this angle, the lower the velocity of the matter in the gas stream. On average, $\beta_1 \sim 19^\circ-24^\circ$, but it increases to 28° in set 6. An indirect indication of a reduced rate of matter outflow from the secondary is the decrease in the size and temperature of the hot spot in the second group of observations and the change in the hot-line parameters. Unfortunately, the amount of data is insufficient for us to draw definite conclusions.

9. MAIN CONCLUSIONS

Let us summarize the main results of this study.

1. We have obtained photometric observations of the cataclysmic variable SDSS J150240.98 + 333423.9/NZ Boo in the V filter at the end of an outburst, $\sim 350-370$ cycles after the outburst onset near April 1, 2012, and in quiescence. Our observations can be subdivided into two groups, the first covering

an interval of ~ 140 orbital cycles and the second an interval of ~ 20 cycles $\sim 500P_{\text{orb}}$ after the first group. The system's brightness level corresponded to quiescence.

2. The system's light curves folded with the orbital period demonstrate that (a) the eclipse depth varies by $\sim 1^m$, (b) the out-of-eclipse brightness level of the system varies by $\sim 0.3^m$, and (c) the flux in the region of the orbital hump also varies by $\sim 0.3^m$.

3. The orbital period changed only insignificantly during the more than 37 200 orbital cycles since the observations reported in [3]: $\Delta P_{\text{orb}}/P_{\text{orb}} < 2 \times 10^{-5}$.

4. We have determined the parameters of the accretion disk, hot line, and other components of J1502 using a combined model for a cataclysmic variable that takes into account the radiation from a hot spot on the leeward side of the gas stream together with radiation from the hot line.

5. Our analysis of variations of the disk parameters derived (its radius R_d , α_g , and temperature T_{in} in the boundary layer) testifies to smooth variations of these parameters between outbursts. In the first group of data, the disk radius and the temperature in its inner regions decreased, and the radial temperature distribution approached the distribution expected for the stationary case; the opposite is observed during the second group of observations, $\sim 500P_{\text{orb}}$ later.

ACKNOWLEDGMENTS

The authors thank A.A. Bykov and V.G. Metlov for their assistance during the observations at Moscow State University Crimean station. This study was supported by the Russian Foundation for Basic Research (grant 14-02-00825) and the Program of State Support for Leading Scientific Schools of the Russian Federation (grant NSh-1675.2014.2).

REFERENCES

1. T. Kato, A. Imada, M. Uemura, D. Nogami, H. Maehara, R. Ishioka, H. Baba, K. Matsumoto, H. Iwamatsu, K. Kubota, K. Sugiyasu, Y. Soejima, Y. Moritani, T. Ohshima, H. Ohashi, J. Tanaka, M. Sasada, A. Arai, K. Nakajima, S. Kiyota, K. Tanabe, K. Imamura, N. Kunitomi, K. Kunihiro, H. Taguchi, M. Koizumi, N. Yamada, Y. Nishi, M. Kida, S. Tanaka, R. Ueoka, H. Yasui, K. Maruoka, A. Henden, A. Oksanen, M. Moilanen, P. Tikkanen, M. Aho, B. Monard, H. Itoh, P. A. Dubovsky, I. Kudzej, R. Dancikova, T. Vanmunster, J. Pietz, G. Bolt, D. Boyd, P. Nelson, Th. Krajci, L. M. Cook, K. Torii, D. R. Starkey, J. Shears, L.-T. Jensen, G. Masi, T. Hynek, R. Novák, R. Kocián Radek, L. Král, H. Kučáková, M. Kolasa, P. Šťastný, B. Staels, I. Miller, Y. Sano, P. de Ponthière, A. Miyashita, T. Crawford, S. Brady, R. Santallo, T. Richards,
2. B. Martin, D. Buczynski, M. Richmond, J. Kern, S. Davis, D. Crabtree, K. Beaulieu, T. Davis, M. Aggleton, E. Morelle, E. P. Pavlenko, M. Andreev, A. Baklanov, M. D. Koppelman, G. Billings, L. Urbančok, Y. Ögmen, B. Heathcote, T. L. Gomez, I. Voloshina, A. Retter, K. Mularczyk, K. Złoczewski, A. Olech, P. Kedzierski, R. D. Pickard, C. Stockdale, J. Virtanen, K. Morikawa, F.-J. Hamsch, G. Garradd, C. Gualdoni, K. Geary, T. Omodaka, N. Sakai, R. Michel, A. A. Cárdenas, K. D. Gazeas, P. G. Niarchos, A. V. Yushchenko, F. Mallia, M. Fiaschi, G. A. Good, S. Walker, N. James, K.-I. Douzu, W. M. Julian II, N. D. Butterworth, S. Yu. Shugarov, I. Volkov, S. Chochol, N. Katysheva, A. E. Rosenbush, M. Khramtsova, P. Kehusmaa, M. Reszelski, J. Bedient, W. Liller, G. Pojmański, M. Simonsen, R. Stubbings, P. Schmeer, E. Muylaert, T. Kinnunen, G. Poyner, J. Ripero, and W. Kriebel, *Publ. Astron. Soc. Jpn.* **61**, S395 (2009).
3. P. Szkody, A. Henden, M. Agüeros, S. F. Anderson, J. J. Bochanski, G. R. Knapp, L. Mannikko, A. Mukadam, N. M. Silvestri, G. D. Schmidt, B. Stephanik, T. K. Watson, A. A. West, D. Winget, M. A. Wolfe, J. C. Barentine, J. Brinkmann, H. J. Brewington, R. A. Downes, M. Harvanek, S. J. Kleinman, J. Krzesinski, D. Long, E. H. Neilsen, A. Nitta, D. P. Schneider, S. A. Snedden, and W. Voges, *Astron. J.* **131**, 973 (2006).
4. J. Shears, T. Campbell, J. Foote, R. Garrett, T. Hager, W. Mack Julian, J. Kemp, G. Masi, I. Miller, J. Patterson, M. Richmond, F. Ringwald, G. Roberts, J. Ruiz, R. Sabo, and W. Stein, *J. Brit. Astron. Assoc.* **121**, 96 (2011).
5. S. P. Littlefair, V. S. Dhillon, T. R. Marsh, B. T. Gänsicke, J. Southworth, I. Baraffe, C. A. Watson, and C. Copperwheat, *Mon. Not. R. Astron. Soc.* **388**, 1582 (2008).
6. C. D. J. Savoury, S. P. Littlefair, V. S. Dhillon, T. R. Marsh, B. T. Gänsicke, C. M. Copperwheat, P. Kerry, R. D. G. Hickman, and S. G. Parsons, *Mon. Not. R. Astron. Soc.* **415**, 2025 (2011).
7. S. P. Littlefair, V. S. Dhillon, T. R. Marsh, B. T. Gänsicke, I. Baraffe, and C. A. Watson, *Mon. Not. R. Astron. Soc.* **381**, 827 (2007).
8. T. Kato, VSNET alert No. 4591, <https://groups.yahoo.com/neo/groups/vsnet-alert/conversations/messages/4591> (2012).
9. T. Kato, VSNET alert No. 4592, <https://groups.yahoo.com/neo/groups/vsnet-alert/conversations/messages/4592> (2012).
10. D. V. Bisikalo, A. A. Boyarchuk, O. A. Kuznetsov, and V. M. Chechetkin, *Astron. Rep.* **41**, 786 (1997).
11. D. V. Bisikalo, A. A. Boyarchuk, O. A. Kuznetsov, V. M. Chechetkin, T. S. Khruzina, and A. M. Cherepashchuk, *Astron. Rep.* **42**, 33 (1998).
12. D. V. Bisikalo, A. A. Boyarchuk, V. M. Chechetkin, O. A. Kuznetsov, and D. Molteni, *Mon. Not. R. Astron. Soc.* **300**, 39 (1998).
13. D. V. Bisikalo, A. A. Boyarchuk, P. V. Kaigorodov, and O. A. Kuznetsov, *Astron. Rep.* **47**, 809 (2003).

13. M. Makita, K. Miyawaki, and T. Matsuda, *Mon. Not. R. Astron. Soc.* **316**, 906 (2000).
14. K. Sawada and T. Matsuda, *Mon. Not. R. Astron. Soc.* **255**, 17P (1992).
15. Z. Kopal, *Close Binary Systems* (Chapman and Hall, London, 1959).
16. T. S. Khruzina, *Astron. Rep.* **55**, 425 (2011).
17. T. S. Khruzina, *Astron. Rep.* **44**, 446 (2000).
18. N. I. Shakura and R. A. Sunyaev, *Astron. Astrophys.* **24**, 337 (1973).
19. T. S. Khruzina, A. M. Cherepashchuk, D. V. Bisikalo, A. A. Boyarchuk, and O. A. Kuznetsov, *Astron. Rep.* **47**, 214 (2003).
20. W. H. Press, B. P. Flannery, and S. A. Teukolsky, *Numerical Recipes. The Art of Scientific Computing* (Cambridge Univ. Press, Cambridge, 1986).
21. D. Himmelblau, *Applied Nonlinear Programming* (McGraw-Hill, New York, 1972; Mir, Moscow, 1975).
22. T. S. Khruzina, *Astron. Rep.* **42**, 180 (1998).
23. D. V. Bisikalo, A. A. Boyarchuk, P. V. Kaigorodov, O. A. Kuznetsov, and T. Matsuda, *Astron. Rep.* **48**, 588 (2004).

Translated by N. Samus'